JOURNAL OF PROPULSION AND POWER
Vol. 23, No. 1, January–February 2007

Simulation of Flow and Mixing from a Cryogenic Rocket Injector

V. Gautam* and A. K. Gupta†
University of Maryland, College Park, Maryland 20742

DOI: 10.2514/1.19731

The effects of confinement, momentum ratio, and recess on the global flow and mixing characteristics of a cryogenic liquid nitrogen stream surrounded by a coaxial gaseous jet from a simulated rocket injector are presented. High-speed cinematography was used to examine the dynamic behavior of the liquid nitrogen jet, whereas infrared thermal imaging was used to demonstrate the cooling effect from the liquid nitrogen jet on the surrounding gases and entrained air moisture. Furthermore, high-speed schlieren imaging was used to examine the effect of momentum ratio on the destabilization of the liquid nitrogen jet before its breakup and eventual mixing with the surrounding gases. The experimental results showed that the liquid nitrogen jet disperses into ligaments and droplets before its vaporization. For the confined conditions, the liquid nitrogen core persists over longer distances downstream of the injector exit before full vaporization. Confinement also reduces the entrainment of the surrounding air as well as the transfer of heat from the surroundings. The liquid nitrogen jet was found to expand earlier and reduced destabilization and mixedness with the surrounding gases with increase in momentum ratios of the coaxial jets. Changing the recess length in the injector had a negligible effect on the liquid nitrogen jet close to the injector exit. However, at downstream locations the recess length provided significant effect on the jet expansion and entrainment of surrounding air. The effect of momentum ratio was also examined quantitatively using the particle image velocimetry diagnostics but using gas/gas (i.e., single-phase) conditions. The results showed the effect of the momentum ratio of the two coaxial gas flows on the subsequent flowfield development and mixing.

I. Introduction

HIGH thrust-to-weight ratio and consistent performance over a range of operating conditions make cryogenic rocket engines one of the best options for space propulsion. However, the scope of space missions is becoming more demanding and so are the requirements of rocket engine performance. To help improve the performance of current rocket engine combustors, several key issues need to be considered. The objective of this paper is to analyze some of the key issues related to the fuel-oxidizer flowfield and mixing in cryogenic rocket engine injectors at atmospheric pressures, so that the results can be used to simulate the conditions before ignition and combustion.

Injector performance is one of the most important issues related to the development of a new generation of rocket engines because of its strong impact on the rocket engine performance and reliability. The development of an optimum injector for a rocket engine requires multiple considerations, such as efficient fuel-oxidizer mixing, quick ignition, combustion stability, thermal compatibility, size, weight, losses, and ease of manufacturing. Among these factors, one of the most critical is efficient fuel-oxidizer mixing, because it directly impacts the other important factors. In the case of cryogenic propellants, efficient mixing becomes even more critical due to the simultaneous presence of liquid and gaseous phases inside the chamber. The liquid jet is required to destabilize, disintegrate, and evaporate quickly to achieve good mixing before ignition and combustion. The destabilization of the liquid jet in a two-phase coaxial flow takes place because of several complex physical processes, such as development of a shear layer from the velocity gradient, turbulent interactions and vorticity produced by boundary layer, and interaction between inertial, surface tension, and viscous forces. Because it is still very difficult to accurately study the combined effects of all parameters analytically or numerically, due to their complex interdependencies and the large uncertainties associated with each parameter, experimental techniques are considered more reliable and accurate to determine the mixing behavior and injector performance [1–5].

Cryogenic rocket injectors can be classified into several categories based on their configuration. The most common classification is impinging vs nonimpinging. In the case of an impinging injector, mixing takes place by direct impingement of the fuel and oxidizer streams, which are aligned at an acute angle to each other. A nonimpinging injector, on the other hand, takes the form of a coaxial element where the fuel and oxidizer streams flow in parallel. In this case, mixing takes place through the development of a shear layer. Coaxial injectors are often preferred to other injector designs because of their simpler design, lower pressure losses, and better combustion stability. The inner flow in a coaxial injector is generally liquid (LOX), whereas the outer one is gaseous (GH_2). Table 1 shows some typical operating conditions for a characteristic coaxial liquid rocket injector [3–5].

Although much research has been conducted lately on cryogenic propellant injection to improve the understanding of the fuel-oxidizer mixing and combustion processes inside rocket engines, our understanding of the mixing and ignition is still primitive. Pal et al. [6] studied the size and distribution of the LOX droplets under reacting conditions and investigated the droplet behavior under nonreacting conditions, as well, with water as a stimulant. Vingert et al. [7] studied the high-pressure injection and mixing processes of cryogenic propellants under nonreacting conditions using LN_2 as a stimulant for LOX. Mayer et al. [8–11] studied the mixing and combustion processes of cryogenic propellants experimentally under sub- and supercritical conditions using optical diagnostic techniques. They observed the vaporization, mixing, and combustion phenomena of the propellants at high chamber pressures of up to 10 MPa. They also analyzed the high-pressure injection and mixing processes of cryogenic propellants under nonreacting conditions using LN_2 and gaseous helium (He) as stimulants. Candel et al. [12,13] studied the sub- and transcritical combustion of cryogenic propellants using laser diagnostic techniques. In a more recent study,

Received 28 August 2005; revision received 21 February 2006; accepted for publication 23 February 2006.

*Graduate Student, Mechanical Engineering Department, Student Member AIAA.

†Professor, Mechanical Engineering Department, Fellow AIAA.

Table 1 Some typical operating conditions for characteristic coaxial rocket engine injectors

Propellant (liquid/gas)	Typical velocities, m/s (liquid/gas)	Velocity ratio (liquid/gas)	Momentum ratio (liquid/gas)	Mixture ratio (liquid/gas)
LOX/H_2	(20–40)/(200–400)	0.05–0.1	0.1–0.2	5–10
LOX/CH_4	(10–20)/(50–100)	0.1–0.2	0.1–0.2	1–5

Oschwald et al. [14] investigated the effect of chamber pressure, initial jet temperature, and acoustic waves on the atomization, mixing, and combustion phenomena of LOX/H_2 coaxial rocket injectors. They also compared their work with some of the previous research conducted on this topic. However, in spite of these numerous research efforts, the atomization, evaporation, mixing, and ignition behavior of cryogenic propellants under all operating conditions, i.e., from below atmospheric to superatmospheric conditions, is still relatively unpredictable.

In general, the flowfield from a typical coaxial injector can be divided into three different zones. The first zone, located close to the injector exit, is known as the initial merged zone. In this zone both the inner liquid core and the outer gaseous one are present with very little or almost no interaction between one another. The expansion of the jets is also very little in this zone. The second or intermediate merged zone is the zone where the inner liquid core starts breaking into large ligamentlike structures that vaporize quickly. Shear layer development and primary mixing between the inner and outer flows take place in this zone; thus, it is considered a very important zone from the ignition point of view. The third and final zone, also known as the fully merged zone, is characterized by complete breakup of the inner liquid core into smaller ligaments and droplets that vaporize and expand very rapidly. In this zone, the flow is fully developed, and secondary mixing between the two fluids takes place. Thus, this zone is considered important to achieve high combustion efficiency and intensity, which results in compact combustor size [14,15].

The shapes and sizes of the discussed mixing zones depend on several parameters, such as the physical and chemical characteristics of the propellants, the velocity ratio between the inner and outer jets, the inlet temperature of the propellants, the geometry of the injector exit, the ambient temperature and pressure inside the mixing chamber, and the momentum flux ratio between the jets. Gautam and Gupta [15], Strakey et al. [16], Villermaux and Rehab [17,18], and Lasheras and Hoppfinger [19] showed that the momentum flux ratio (defined as $\mathrm{MR} = \sqrt{\rho_1 v_1^2/\rho_2 v_2^2}$) is one of the key parameters for single-phase or two-phase coaxial-jet mixing. They also showed that the length of the inner potential core, as well as the shapes and sizes of the various zones, is significantly affected by the momentum flux ratio.

Because cryogenic rocket propellants have extremely distinct flow characteristics compared with gaseous propellants, it is necessary to implement new experimental designs and techniques to quantify the flow behavior and mixing performance. High-speed cinematography, schlieren imaging, infrared thermal imaging, and particle image velocimetry (PIV) have been used in this work to examine the flow and mixing characteristics of a single coaxial injector and to simulate the characteristic rocket injector performance before ignition. The experimental results obtained here assist in better understanding of the flow behavior and mixing from rocket engine injectors. Besides, the results obtained can also be used to validate numerical models under nonreacting flow conditions.

II. Experimental Setup and Conditions

The test rig consists of a coaxial injector and a downstream mixing chamber of square cross section, as shown in Fig. 1. The injector has an adjustable recess length. The inner tube diameter of the injector is $D = 0.33$ in. with a wall thickness of 0.02 in. The inner diameter of the outer tube is 0.5 in. The mixing chamber has a side length of 1 in. and a height of 13 in. Gaseous N_2, helium (He), or CO_2 are supplied through the outer annulus of the injector whereas LN_2 flows through the inner tube. In this study, LN_2 was used to simulate LOX because LN_2 is chemically inert, easy and safe to install for laboratory testing, and environmentally benign. Table 2 shows some of the physical properties of LN_2 and LOX. It can be seen that the values of the boiling temperature, viscosity, and surface tension are close; thus, the liquid breakup into ligaments and droplets will be similar for both fluids. The experimental test matrix of the flow conditions examined here is given in Table 3.

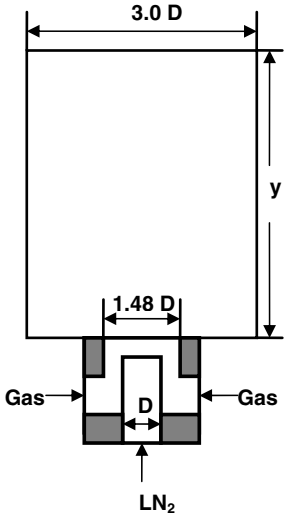

Fig. 1 Schematic diagram of the test coaxial injector.

High-speed cinematography, schlieren imaging, and IR thermal imaging were used to examine the global flow features of the LN_2 jet in a surrounding gaseous stream. The entrainment of the ambient air into the jet was also investigated by confining the flow, wherein two cases of confined and semiconfined were considered. For the latter, the jet was confined from two opposite sides, thus leaving the other two sides of the chamber unconfined. This configuration can thus simulate injector-wall interaction.

Time-resolved images of the LN_2 jet flow were acquired at 512 frames/s with a resolution of 1024×1024 pixels. Thermal images of the flow were captured using a long range (8–9 μm) infrared camera equipped with a quantum wall infrared photon detector to analyze the infrared light emitted from the cold flow and its warmer surroundings. The radiance captured by the infrared camera depends mainly on the object temperature, background temperature, and the emissivity of the source object. For an opaque source object at temperature T and emissivity ε, and for a background temperature T_b, the total radiance L captured is given by

$$L = \varepsilon L_o(T) + (1 - \varepsilon) L_b(T_b) \tag{1}$$

where L is in $\mathrm{W}/(\mathrm{m}^2 \cdot \mathrm{sr})$, $\{\varepsilon L_o(T)\}$ is the radiance emitted by the source, and $\{(1 - \varepsilon) L_b(T_b)\}$ is the radiance reflected off the source due to background emissions. The infrared camera detector measures the captured radiation in Watts, whereas the surface area and solid angles are calculated from the source size, optics aperture, detector size, and the distance between the source and the camera. Several other factors can also affect the radiance captured. These include the ambient temperature, relative humidity, and the transmission of the external optics. The ThermaCAM software of the camera has built-in correction functions for these factors. The net radiance emitted by the source can be calculated from

$$L_o(T) = \frac{1}{\varepsilon}[L - (1 - \varepsilon) L_b(T_b)] \tag{2}$$

Table 2 Some physical properties of LOX and LN_2

Fluid	Density	Boiling point	Surface tension	Viscosity
LOX	1141 kg/m^3	−183°C (90 K)	0.0132 N/m	0.000197 Pa*s
LN_2	808 kg/m^3	−196°C (77 K)	0.0089 N/m	0.000163 Pa*s

Table 3 Test matrix of the examined flow conditions

Case #	Inner tube (liquid)	Outer annulus (gaseous)	Recess length, in.	Inlet Velocity, m/s (inner/outer)	Mom. ratio (inner/outer)
1	LN_2	He (7°C)	0	11/19.5	40
2	LN_2	N_2 (7°C)	0	11/19.5	15
3	LN_2	N_2 (7°C)	0.1	11/19.5	15
4	LN_2	N_2 (7°C)	0.2	11/19.5	15
5	LN_2	CO_2 (7°C)	0	11/19.5	12
6	LN_2	He (7°C)	0	5/42	8
7	LN_2	N_2 (7°C)	0	5/42	3

Once this net radiance is known, the camera software calculates the corresponding temperature from a digitally stored calibration lookup table. The images presented here were captured at a frequency of 60 Hz, and they represent the average of 300 instantaneous images.

The effect of momentum ratio on mixing was examined using the PIV technique under single-phase gaseous flow conditions. A different coaxial injector was used for this purpose with a central tube of 0.8 mm inner diameter surrounded by a 12.89 mm i.d. outer tube. This geometry allowed examination of large range of momentum flux ratios between the inner and outer jets. The results demonstrated here are only for the momentum ratios of 0.69 and 0.81. At higher momentum ratios, the effect was even more significant. Detailed flow dynamics and strain rates have been obtained for the shown momentum ratios.

A two-dimensional (2-D) PIV system was used to examine the features of the flowfield. The test section was illuminated by means of a solo PIV Nd:YAG laser. Submicron glass balloon particles were introduced into the annular flow using a fluidized bed. A charged coupled device camera with an active pixel array of 1280×1024 was used to record the images. The camera, placed normal to the laser sheet, was operated by a control module for image acquisition. The camera was equipped with mechanical shutters and a narrow bandpass filter (0.87 nm) at a center wavelength of 532 nm to allow for maximum transmission of the signal, thus enhancing the recorded images of the particles present in the gas flow. The frequencies of the laser and the camera were synchronized at 5 Hz. The measured area in the test section was 30×45 mm in the radial and axial directions (x and y), respectively. Five hundred image pairs were acquired for each case to determine the mean and turbulence properties associated with the flowfield.

III. Results and Discussion

A. Global Flowfield Data with Liquid Nitrogen

The goal of this study is to examine the flow and mixing characteristics of an LN_2 flow surrounded by a coaxial gaseous jet, to simulate the flows from rocket engine injectors. Therefore, the effects of jet confinement, momentum flux ratio, and the recess length of the LOX post on the flow expansion, heat transfer, and the entrainment of the surrounding air have been investigated.

Figure 2a shows an image of an unconfined LN_2 jet in a coaxial GN_2 stream. This image has been extracted from a high-speed clip taken at 500 frames/s. The close-up view of the flow, shown in Fig. 2b, is an image from a clip taken at 1000 frames/s. The evolutionary behavior of the LN_2 jet in a coaxial gaseous stream can be seen. The expansion of the jets and its effect on the surrounding entrained air can also be visualized. The dense white fog, visible downstream of the injector exit, is due to the rapid condensation and freezing of the moisture present in the surrounding air that gets entrained into the gaseous jet. Although the presence of this white fog around the LN_2 stream deteriorates the visibility of the jet, one can still observe that it disperses into ligaments and droplets before its vaporization further downstream, where it eventually mixes with the surrounding gas.

Because mixing and combustion takes place in a confined environment in all practical systems, the effect of confinement on the global flow characteristics has also been examined. Figure 3 shows the effect of confinement on the LN_2/GN_2 flow for three different cases: a) unconfined, b) semiconfined (two sides confined), and c) fully confined. The visibility in Fig. 3c is poor because two sides of the confinement had metallic bars, which allowed for very little light to illuminate the flow. The dark stripes between $y/D = 10$ and $y/D = 15$ are the shadow of clamps used to hold together the confinement walls of the chamber. Nevertheless, the impact of confinement on the evolution of the LN_2 flow can still be observed. An examination of these images shows the significant effect of

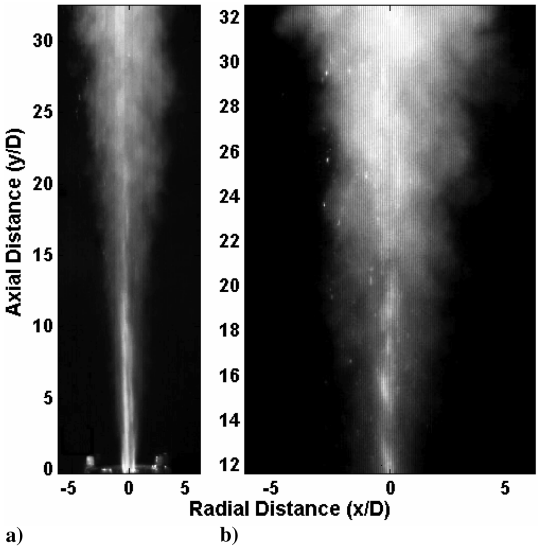

Fig. 2 High-speed images of unconfined LN_2/GN_2 flow with no recess; a) 500 frames/s, b) 1000 frames/s.

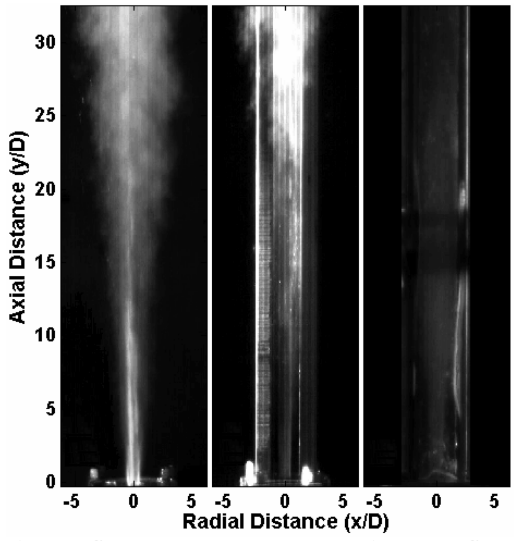

Fig. 3 High-speed images of LN_2/GN_2 flow with no recess for three different cases.

confinement on the flow expansion, mixing, and heat exchange with the surrounding gases. The LN_2 jet persists over longer distances for the semiconfined and fully confined cases as compared with the unconfined case. This suggests that the vaporization and expansion of the LN_2 jet are reduced with confinement. Significantly less white fog is also observed around the LN_2 jet downstream of the injector exit in the fully confined case, which means less entrainment of the surrounding air into the gaseous flow. For the confined case, the LN_2 jet does not even fully disperse within the shown section of the mixing chamber. Droplets of LN_2 could be recognized near the injector exit, which suggests reduced heat transfer from the surroundings to the LN_2 jet.

To further assess the flow behavior and mixing, infrared (IR) thermal images of the flow were taken to analyze the cooling effect of the LN_2 jet (leaving the injector exit at 77 K) on the surrounding gases and the entrained air moisture. The minimum temperature that can be measured accurately by the IR camera is −20°C, and the surrounding atmospheric temperature was set to 25°C. Although LN_2 has an emissivity close to 1.0, whereas the emissivity of the surrounding gases is about 0.05, the calculation of temperature was done inside the ThermaCAM camera software using a single value of the emissivity of 0.05 for all the data presented here. As can be seen from Eq. (2), the value of the emissivity affects the absolute values of the detected temperatures only and not the temperature gradients inside the flow. The reason behind choosing the value of 0.05 for the overall emissivity is that the gas-phase mixing is considered more important because this contributes directly to mixture ignition.

Figures 4a and 4b show IR thermal images of the LN_2/GN_2 flow for the unconfined and semiconfined cases, respectively. The LN_2 jet leaving the injector appears warm when its temperature is, in fact, cryogenic, because of the large reflection of light from the liquid surface, which suggests little or no interaction of the LN_2 jet with the surrounding gases in this region. This region is designated as the initial merged zone as discussed earlier. As the flow progresses, it starts vaporizing and mixing with the surrounding gas. The cooling effect from the LN_2 jet on its surroundings is recognizable from the increasing darkness of the flow's gray shade. Further downstream, the flow appears much darker due to the cold gaseous flow and the condensed moisture of the surrounding air. The effect of confinement on the LN_2 jet can be seen in Fig. 4b. The length of the warm appearing LN_2 jet is increased significantly for the semiconfined case which suggests that it persists over a longer distance as compared with the unconfined case. The sidebars are warmer near the injector exit than they are further downstream, which shows the low cooling effect from the LN_2 jet in that region. The sidebars and the surrounding gases become colder as the flow progresses downstream due to the vaporization and mixing of the LN_2 jet with the surrounding gases. The colder regions of the flow are reduced

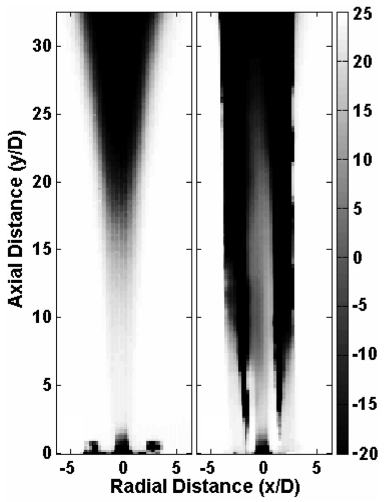

a) Unconfined b) Semiconfined

Fig. 4 Temperature distribution (°C) of LN_2/GN_2 flow with no recess for two cases.

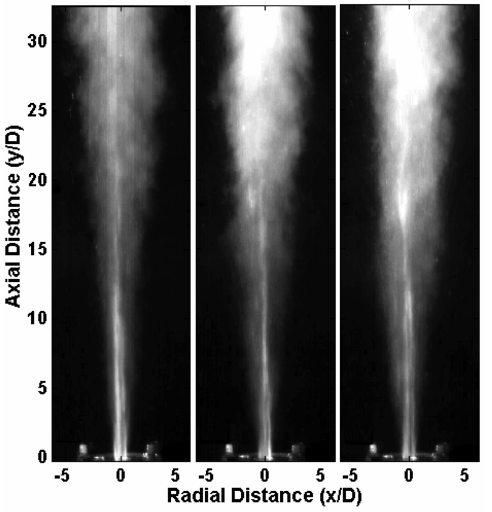

a) No recess b) 0.1 in. recess c) 0.2 in. recess

Fig. 5 High-speed images of LN_2/GN_2 flow for three different cases.

significantly as compared with the unconfined case, which confirms the reduction in the cooling effect from the LN_2 jet and reduced entrainment of the surrounding air into the annular gaseous jet. An IR thermal image of the fully confined case was not taken because the quartz glass of the mixing chamber inhibits IR radiation from passing through.

Recess is used in most coaxial injectors to enhance the combustion stability. A qualitative assessment of the effect of recess on evaporation and mixing of the LN_2 jet in a coaxial gaseous jet has been conducted in this work. Figure 5 shows high-speed images of the LN_2/GN_2 flow for three different recess cases: a) no recess, b) 0.1 in. recess length, and c) 0.2 in. recess length. Slight increases in jet expansion can be observed at locations closer to the injector exit. Moreover, the density of the white fog (frozen moisture) increases with increase in distance downstream of the injector exit which suggests higher entrainment of the surrounding air into the jet as well as stronger cooling effect from the LN_2 jet with increased recess length.

Figure 6 shows IR thermal images of the LN_2/GN_2 flow for the three different recess length cases described in the preceding paragraph. The images look very similar at the locations close to the injector exit. This suggests that changing the recess length does not affect the evaporation of the LN_2 jet much at early stages of the flow evolution. However, further downstream, the recess length shows a

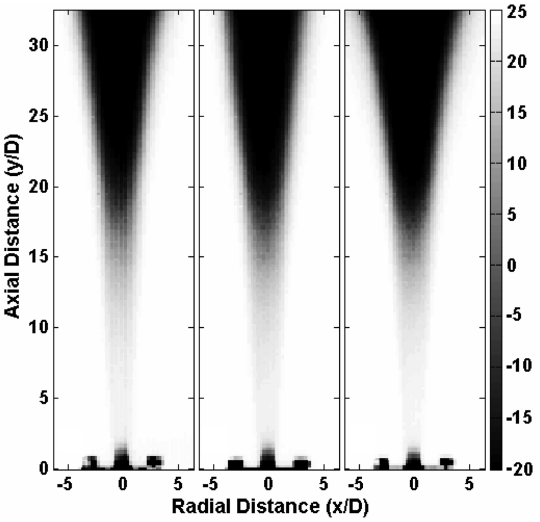

a) No recess b) 0.1 in. recess c) 0.2 in. recess

Fig. 6 Temperature distribution (°C) of LN_2/GN_2 flow for three different cases.

significant effect on the expansion of the jets as well as entrainment of the surrounding air. The colder (darker) region of the flow widens significantly with an increase in recess length at downstream locations from the injector exit. This shows higher expansion of the jets as well as higher entrainment of the surrounding air into the jet. These results provide further support and confirmation to the data obtained using high-speed cinematography.

Experimental data were obtained to examine the effect of momentum ratio on the global features of the LN_2 jet flowing inside different coaxial gaseous jets (i.e., different momenta of the LN_2 jet to outer jet). The momentum flux ratio is defined here as $MR = \sqrt{\rho_1 v_1^2/\rho_2 v_2^2}$, where ρ_1 and v_1 are the density and velocity of inner jet (LN_2), respectively, whereas ρ_2 and v_2 are those of the annular gaseous jet, respectively. For the present injector geometry, the momentum flux ratio and the momentum ratio are the same, because the cross-sectional areas of the two jets are equal. Figure 7 shows the effect of three different momentum ratios on the subsequent high-speed images, namely, a) $MR = 12(LN_2/CO_2)$, b) $MR = 15(LN_2/GN_2)$, and c) $MR = 40(LN_2/He)$. The volumetric flow rates of the gaseous flows were kept equal, so that different momentum ratios are associated with different densities of the coaxial gases. As can be seen from Fig. 7, the central LN_2 jet persists over longer distances at higher momentum flux ratios, which suggests reduced mixing with the surrounding gas and, subsequently, lower heat transfer. The entrainment of the surrounding air into the annular gaseous jet starts closer to the injector exit for higher momentum flux ratio, which suggests reduced mixing with the surrounding gas and, subsequently, lower heat transfer. The entrainment of the surrounding air into the annular gaseous jet starts closer to the injector exit for higher momentum flux ratio, which is revealed by the evolution of the dense white fog. This behavior is attributed to the change in density of the annular gaseous jet.

The last set of thermal images presented in Fig. 8 is for the same momentum ratios depicted in Fig. 7. It can be observed that the cooling effect from the LN_2 jet on the surrounding gases starts earlier for the lower momentum ratio case because the length of the warm appearing section of the LN_2 jet (where there is almost no interaction with the surrounding gases) is reduced for the smaller momentum ratio case. This implies faster evaporation of the LN_2 jet and more mixing with the surrounding gases for the lower momentum ratio case.

To further examine the effect of recess and momentum ratio, axial and radial temperature distributions were plotted. Figure 9a shows the centerline temperature distributions for the five investigated recess length and momentum ratio cases. It can be seen that recess length has very little effect on the centerline temperature distribution

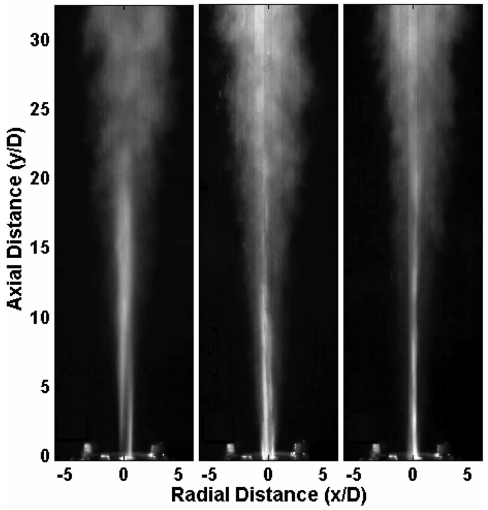

a) MR=12 b) MR=15 c) MR=40

Fig. 7 High-speed images of LN_2/Gas flow with no recess for three different momentum ratios.

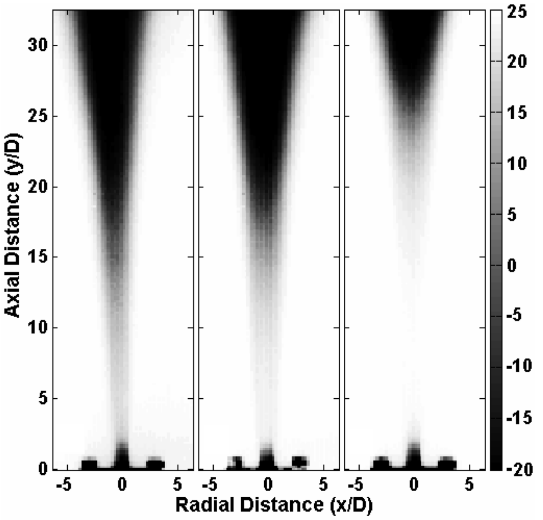

a) MR=12 b) MR=15 c) MR=40

Fig. 8 Temperature distribution (°C) of LN_2/Gas flow with no recess for three different momentum ratios.

close to injector exit. However, it does affect the LN_2 flow at downstream locations; this can be seen from the differences in temperature distribution after around 15 diameters downstream of the injector exit. In contrast, the results show significant effect of momentum ratio on the centerline temperature distribution. The colder temperature region moves closer to the injector exit with a decrease in momentum ratio. This suggests faster evaporation of LN_2 jet and more mixing with the surrounding gases with decrease in momentum ratio. Figure 9b provides a plot of the radial temperature distribution at an axial location of $y/D = 30$. At this location, no significant effect of the momentum ratio on the temperature distribution can be observed. The colder region reduces slightly in size for the $MR = 40$ case, which suggests less cooling of the surrounding gases and reduced mixing. On the other hand, recess length has a significant effect on the radial temperature distribution. The colder region broadens for larger recess lengths, which suggests higher jet expansion and more entrainment of the surrounding gases, as concluded previously.

A high-speed schlieren imaging technique was used to examine the development of the shear layer between the two fluids and its impact on the destabilization of the cryogenic jet. Figure 10 shows the effect of changing momentum ratio on the evolutionary behavior of shear layer development between the two flows and destabilization of the cryogenic jet. The three examined cases are a) $MR = 8(LN_2/He)$, b) $MR = 3(LN_2/GN_2)$, and c) $MR = 2.5(LN_2/CO_2)$. The flow conditions examined in this experiment are slightly different than the previous cases because it was difficult to accurately quantify the jet destabilization frequencies for previous cases. One can clearly see a stable liquid jet emerging from the injector exit surrounded by a gaseous jet. As the flow progresses further downstream, the formation of vortical structures from shear layer development causes the inner liquid core to break up and mix with the surrounding gases. For the GN_2 and CO_2 cases, the presence of two different flows close to the injector exit could not be seen because of smaller density gradients between the injected gas and atmospheric air immediately near to the injector exit. The results shown in Fig. 10 clearly show an increase in formation of vortical structures with decrease in momentum ratio between the jets. This suggests faster breakup of the liquid jet and increased mixedness with the surrounding gases at decreased momentum ratios.

The focus in the present experiments was to capture the large size vortical structures inside the flow because they are responsible for the LN_2 jet dispersion. Thus, the intent of the experiments was to capture the smaller frequency structures that appear on the interface between the LN_2 jet and the surrounding gas flow due to coalescence of high frequency structures. Table 4 shows calculated experimental jet destabilization frequencies for the cases discussed in the previous

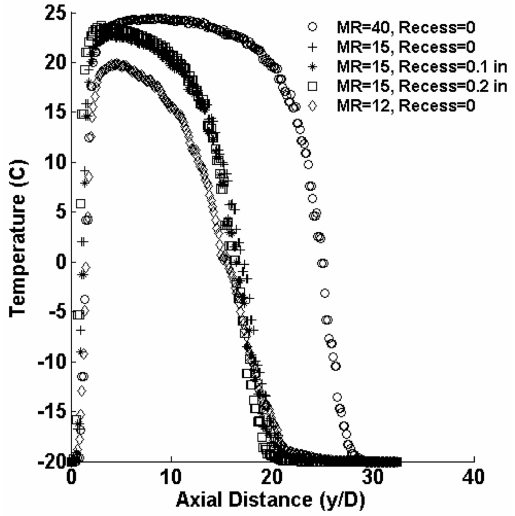

a) Centerline temp distribution

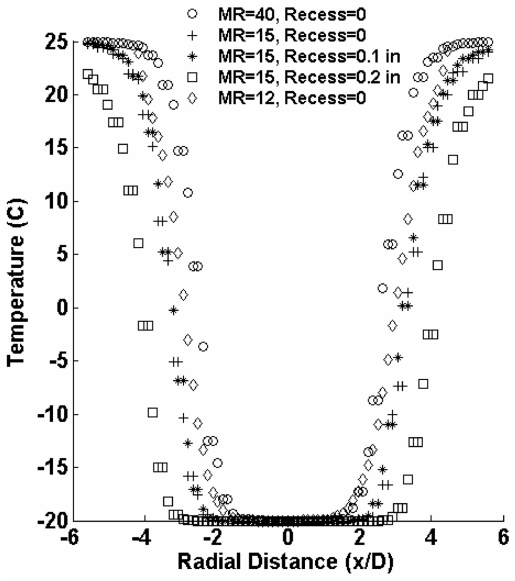

b) Radial temp distribution at y/D=30

Fig. 9 Temperature distributions for different recess and momentum ratio cases (extracted from IR thermal images).

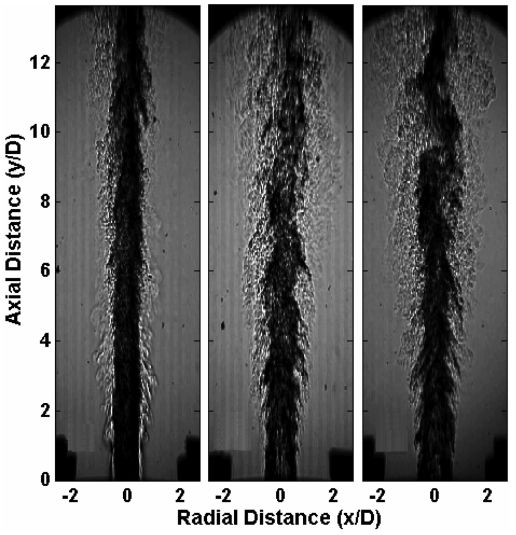

a) MR=8 b) MR=3 c) MR=2.5

Fig. 10 Schlieren images of LN_2/Gas flow with no recess for three different momentum ratios.

paragraph and lie in the range of about 200 to 300 Hz. The corresponding Strouhal number based on inner jet diameter (jet preferred mode) was calculated to be about 0.4, whereas that based on the vorticity thickness of the gas flow [18,19] was calculated to be 2×10^{-3}. These Strouhal numbers are comparable to that reported in the literature ($Sr \sim 0.2$–0.5 for jet preferred mode and about 7.6–8.7×10^{-3} based on vorticity thickness of flow). The sample experimental frequencies are offered here to provide an order of magnitude estimate on the vortical frequencies associated with the flow. The finer scale theoretical frequencies provide the formation of smallest vortical structures that coalesce together to form larger vortical structures and lead to the eventual breakup of liquid jet. An estimate of these frequencies is made from the convective velocity of the flow. The convective velocity u_c of the interface is calculated as $u_c = (\sqrt{\rho_l} \cdot v_l + \sqrt{\rho_g} \cdot v_g)/(\sqrt{\rho_l} + \sqrt{\rho_g})$. The theoretical instability frequencies f_{th} is calculated as $f_{\text{th}} = (u_c/\delta_w)(\rho_g/\rho_l)^{0.5}$ where δ_w is vorticity thickness of gaseous stream [18]. The calculated frequencies were found to be 1266, 6231, and 8710 corresponding to the convective velocity of 5.5, 6.4, and 6.7 m/s, respectively. These theoretical frequencies are much higher than the calculated experimental frequencies, as expected, because the experimentally measured frequencies are from larger vortical structures present in the flow.

A visual observation of the flow revealed that indeed a range of frequencies are present in the flow. Thus, depending on the specific region examined in the flow, different frequencies may be evaluated. Therefore, the calculated experimental frequency from the flow must be taken as a guideline on the low frequency associated with the flow, whereas the theoretical frequency is the primary instability frequency of the liquid jet. These results suggest that the vortical frequencies responsible for liquid jet destabilization and breakup decreased with a decrease in gaseous jet density and momentum ratio. The results also suggest that the jet preferred mode is the dominant destabilization mode for the liquid jet instability for the cases analyzed. These results compare favorably well with the experimental results reported by Villermaux [18] and Lasheras and Hoppfinger [19]. However, further experiments and analysis may be supported to further enrich this conclusion.

B. Shear Layer Mixing

To provide a further quantification on the effect of momentum ratio on flow dynamics and shear layer mixing, 2-D particle image velocimetry diagnostics was carried out. The LN_2 jet was replaced with a gaseous helium stream due to the complexity associated with flow seeding of the cryogenic LN_2 jet required for PIV measurements. The momentum ratio was controlled by using different outer gases (O_2 and CO_2) having different densities, similar to the approach used for the inner LN_2 jet. Even with the use of a gaseous helium jet, similar effects of the momentum ratio were observed. Figures 11a and 11b compare the distributions of the axial velocity associated with the two configurations of He/O_2 and He/CO_2 from the injector, respectively. Significant differences in the velocity decay and the magnitude of maximum velocity can be

Table 4 Destabilization frequencies for some of the examined cases

Case	u_c, m/s	Re_{gas}	f_{ex} (experimental, low frequency)	Strouhal No. ($f_{\text{ex}}D/u_c$)	Strouhal No. ($f_{\text{ex}}\delta_w/u_c$)
6	5.5	2931	245	0.38	0.0028
7	6.4	25104	294	0.39	0.0019
8	6.7	43136	327	0.42	0.0018

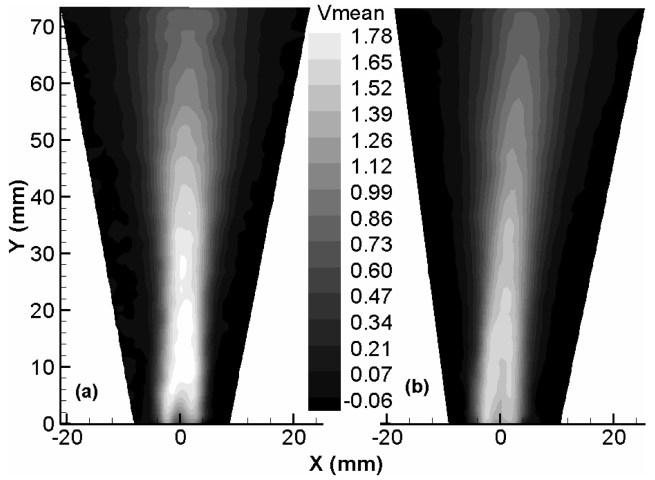

a) He/O_2 (MR=0.81) b) He/CO_2 (MR=0.69)

Fig. 11 Distribution of mean axial velocity associated with two configurations of He/O_2 and He/CO_2.

recognized. The He/O_2 flow case has higher axial velocity than that for the He/CO_2 case but a slightly narrower shear layer region at the downstream locations. This is attributed primarily to the change in momentum ratio between the inner and outer jets. The lower axial velocity associated with the He/CO_2 allows for lower velocity gradients to provide higher shear layer mixing with a decrease in the momentum ratio.

Closer examination of the effect of momentum ratio on the shear layer mixing was conducted by plotting the distributions of axial velocity and shear strain at different axial locations. Figures 12a and 12b show the distributions of axial velocity and shear strain for both flow configurations at $y/D = 0.16$. The profiles of axial velocities are similar to each other, which was expected at this location close to the injector exit. The dips recognizable in the velocity profiles near to the centerline are attributed to the fact that only the outer flow of the injector was seeded and that no significant mixing had occurred at this very early stage of the flow evolution. The shear strain profile shows four distinct peaks because of the existence of two distinct flows in that region. The negative magnitudes of some of the peaks are due to the change in direction of the shear strain. It should be noted that all four peaks are at the same radial location for both flow configurations, as expected. Also, the magnitude of shear strain is higher for the He/O_2 configuration (having higher momentum ratio). As the flow progresses further downstream, the distinction between the profiles of the two flow configurations fades away gradually, which can be seen in Figs. 13a and 13b (e.g., at $y/D = 1.16$). The peaks of axial velocity start to merge, and so do the shear strain, which suggests an increase in mixing between the coaxial jets. Similarly, as one moves further away from the injector exit, the distinct peaks almost completely merge into one another to evolve with the existence of only one flow, as depicted in Figs. 14a and 14b (at $y/D = 2.32$). This suggests that the two flows are completely mixed at this far axial location. The higher magnitudes of axial velocity and shear strain rate associated with the He/O_2 flow at the three axial locations of Figs. 11–13 confirm that mixing and jet expansion are slower at higher momentum ratios.

IV. Conclusions

The experimental results presented here show the effect of confinement, momentum ratio, and recess length on the vaporization and mixing in a coaxial rocket engine injector. Some of the experimental jet destabilization frequencies as well as the characteristic primary instability frequencies present in the coaxial jets have been examined using cryogenic fluid and surrounding gas of different densities. A combination of various nonintrusive diagnostic techniques has provided insightful features of the injector performance characteristics under simulated rocket injector operating conditions before ignition.

The LN_2 jet disperses into ligaments and droplets before vaporization. The confinement reduces the vaporization of the LN_2 jet by increasing the axial distance over which the jet persists before full vaporization. Confinement significantly reduces the entrainment of surrounding gases and heat transfer from the surroundings to the injector fluids.

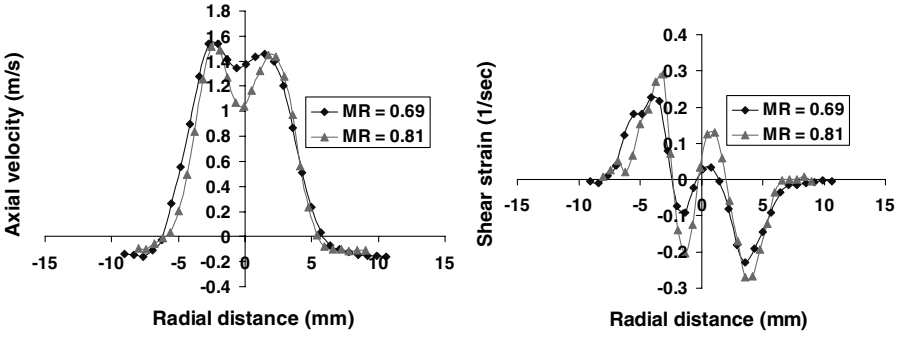

a) Axial velocity distribution b) Shear strain distribution

Fig. 12 Distribution of axial velocity and shear strain at y/D = 0.16.

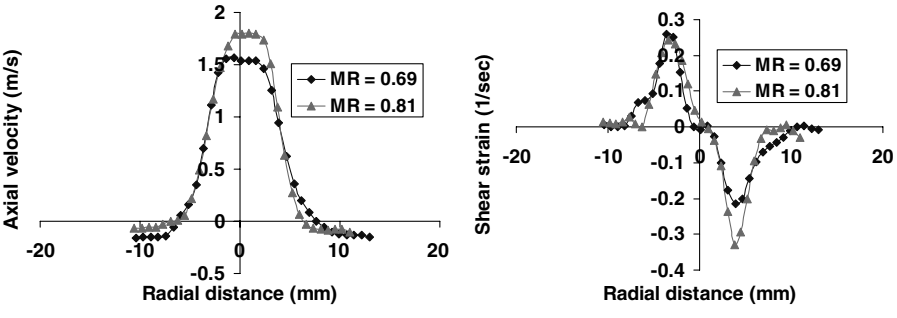

a) Axial velocity distribution b) Shear strain distribution

Fig. 13 Distribution of axial velocity and shear strain at y/D = 1.16.

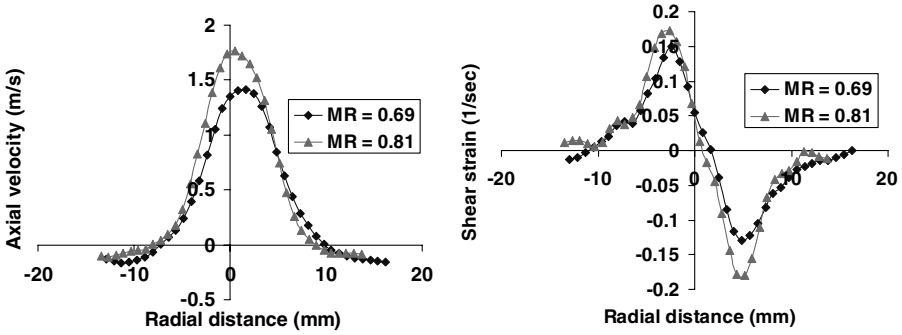

a) Axial velocity distribution **b) Shear strain distribution**

Fig. 14 Distribution of axial velocity and shear strain at y/D = 2.32.

Increase in momentum ratio results in early expansion of the outer gas flow and higher entrainment of the surrounding gases. However, the LN_2 jet persists over longer distances for higher momentum ratios, leading to its reduced mixing with the surrounding gases. The recess length has little effect on the evaporation of the LN_2 jet but affects the expansion of the flow and entrainment of the surrounding gases significantly at downstream locations. The results also revealed an increase in liquid jet instability with decrease in momentum ratio between the inner and outer flows of the injector. The flowfield results obtained from the 2-D PIV diagnostics using gas/gas flows assist in understanding the role of momentum ratio on mixing in LN_2/gas flows. Mixing has been shown to enhance with a decrease in momentum ratio between the inner and outer jets.

Acknowledgments

This work was supported by the Space Vehicle Technology Institute under grant NCC3-989 jointly funded by NASA and U.S. Department of Defense within the NASA Constellation University Institutes Project, with Claudia Meyer as the Project Manager. Support provided by Jakub Gmurczyk and Pierre Rousseau is much appreciated.

References

[1] Sutton, G. P., and Biblarz, O., *Rocket Propulsion Elements*, 7th ed., Wiley, New York, 2001.

[2] Beer, J. M., and Chigier, N. A., *Combustion Aerodynamics*, Applied Science Publishers, London, 1972.

[3] Huzel, D., and Huang, D., *Modern Engineering for Design of Liquid Propellant Rocket Engines*, Vol. 147, Progress in Astronautics and Aeronautics, AIAA, Washington, D.C., 1992, Chap. 4.

[4] Vingert, L., Gicquel, P., Lourme, D., and Menoret, L., *Coaxial Injector Atomization*, Vol. 169, Progress in Astronautics and Aeronautics, AIAA, Washington, D.C., 1994.

[5] Yang, V., Habiballah, M., Popp, M., and Hulka, J., *Liquid Rocket Thrust Chambers: Aspects of Modeling, Analysis, and Design*, Progress in Astronautics and Aeronautics, Vol. 200, AIAA, Reston, VA, 2004, Chaps. 9–10.

[6] Pal, S., Moser, M. D., Ryan, H. M., Foust, M. J., and Santoro, R. J., "Shear Coaxial Injector Atomization Phenomena for Combusting and Non-Combusting Conditions," *Atomization and Sprays*, Vol. 6, No. 2, 1996, pp. 227–244.

[7] Vingert, L., Gicquel, P., Ledoux, M., Care, I., Micci, M., and Glogowski, M., *Atomization in Coaxial Jet Injectors*, Vol. 200, Progress in Astronautics and Aeronautics, AIAA, Reston, VA, 2004, Chap. 3, pp. 105–140.

[8] Mayer, W., and Tamura, H., "Propellant Injection in a Liquid Oxygen/Gaseous Hydrogen Rocket Engine," *Journal of Propulsion and Power*, Vol. 12, No. 6, Nov.–Dec. 1996, pp. 1137–1147.

[9] Mayer, W., Schik, A., Vielle, B., Chauveau, C., Gokalp, I., Talley, D., and Woodward, R., "Atomization and Breakup of Cryogenic Propellants Under High Pressure Subcritical and Supercritical Conditions," *Journal of Propulsion and Power*, Vol. 14, No. 5, Sept.–Oct. 1998, pp. 835–842.

[10] Mayer, W., Schik, A., Schaffler, M., and Tamura, H., "Injection and Mixing Processes in High Pressure Liquid Oxygen/Gaseous Hydrogen Rocket Combustors," *Journal of Propulsion and Power*, Vol. 16, No. 5, Sep.–Oct. 2000, pp. 823–828.

[11] Mayer, W., Ivancic, B., Schik, A., and Hornung, U., "Propellant Atomization and Ignition Phenomena in Liquid Oxygen/Gaseous Hydrogen Rocket Combustors," *Journal of Propulsion and Power*, Vol. 17, No. 4, July–Aug. 2001, pp. 794–799.

[12] Candel, S., Herding, G., Synder, R., Scouflaire, P., Rolon, C., Vingert, L., Habiballah, M., Grisch, F., Pealat, M., Bouchardy, P., Stepowski, D., Cessou, A., and Colin, P., "Experimental Investigation of Shear Coaxial Cryogenic Jet Flames," *Journal of Propulsion and Power*, Vol. 14, No. 5, Sept.–Oct. 1998, pp. 826–834.

[13] Candel, S., Juniper, M., Singla, G., Scouflaire, P., and Rolon, C., "Structure and Dynamics of Cryogenic Flames at Supercritical Pressure," *Combustion Science and Technology*, Vol. 178, Jan. 2006, pp. 161–192.

[14] Oschwald, M., Smith, J. J., Branam, R., Hussong, J., Schik, A., Chehroudi, B., and Talley, D., "Injection of Fluids into Supercritical Environments," *Combustion Science and Technology*, Vol. 178, Jan. 2006, pp. 49–100.

[15] Gautam, V., and Gupta, A. K., "Simulation of Mixing in Rocket Engine Injector under In-Space Conditions," *41st AIAA/ASME/ASME/SAE/ASEE Joint Propulsion Conference*, AIAA Paper 2005-1445, 2005.

[16] Strakey, P. A., Talley, D. G., and Hutt, J. J., "Mixing Characteristics of Coaxial Injectors at High Gas/Liquid Momentum Ratios," *Journal of Propulsion and Power*, Vol. 17, No. 2, March–April 2001, pp. 402–410.

[17] Villermaux, E., and Rehab, H., "Mixing in Coaxial Jets," *Journal of Fluid Mechanics*, Vol. 425, Dec. 2000, pp. 161–185.

[18] Villermaux, E., "Mixing and Spray Formation in Coaxial Jets," *Journal of Propulsion and Power*, Vol. 14, No. 5, Sept.–Oct. 1998, pp. 807–817.

[19] Lasheras, J. C., and Hoppfinger, E. J., "Liquid Jet Instability and Atomization in a Coaxial Gas Stream," *Annual Review of Fluid Mechanics*, Vol. 32, Jan. 2000, pp. 275–308.

C. Avedisian
Associate Editor